Asia-Pac. J. Atmos. Sci., 54(2), 237-251, 2018
DOI:10.1007/s13143-018-0007-1
pISSN 1976-7633 / eISSN 1976-7951

Surface Downward Longwave Radiation Retrieval Algorithm for GEO-KOMPSAT-2A/AMI

Seo-Hee Ahn[1,3], Kyu-Tae Lee[1,2], Se-Hun Rim[1,2], Il-Sung Zo[2], and Bu-Yo Kim[1,2]

[1]*Department of Atmospheric and Environmental Sciences, Gangneung-Wonju National University, Gangneung, Korea*
[2]*Research Institute for Radiation-Satellite, Gangneung-Wonju National University, Gangneung, Korea*
[3]*Division of Polar Climate Sciences, Korea Polar Research Institute, Incheon, Korea*

(Manuscript received 8 March 2017; accepted 30 October 2017)

Abstract: This study contributes to the development of an algorithm to retrieve the Earth's surface downward longwave radiation (DLR) for 2nd Geostationary Earth Orbit KOrea Multi-Purpose SATellite (GEO-KOMPSAT-2A; GK-2A)/Advanced Meteorological Imager (AMI). Regarding simulation data for algorithm development, we referred to Clouds and the Earth's Radiant Energy System (CERES), and the European Centre for Medium-Range Weather Forecasts (ECMWF) ERA-interim reanalysis data. The clear sky DLR calculations were in good agreement with the Gangneung-Wonju National University (GWNU) Line-By-Line (LBL) model. Compared with CERES data, the Root Mean Square Error (RMSE) was 10.14 Wm^{-2}. In the case of cloudy sky DLR, we estimated the cloud base temperature empirically by utilizing cloud liquid water content (LWC) according to the cloud type. As a result, the correlation coefficients with CERES all sky DLRs were greater than 0.99. However, the RMSE between calculated DLR and CERES data was about 16.67 Wm^{-2}, due to ice clouds and problems of mismatched spatial and temporal resolutions for input data. This error may be reduced when GK-2A is launched and its products can be used as input data. Accordingly, further study is needed to improve the accuracy of DLR calculation by using high-resolution input data. In addition, when compared with BSRN surface-based observational data and retrieved DLR for all sky, the correlation coefficient was 0.86 and the RMSE was 31.55 Wm^{-2}, which indicates relatively high accuracy. It is expected that increasing the number of experimental Cases will reduce the error.

Key words: surface downward longwave radiation (DLR), Clouds and the Earth's Radiant Energy System (CERES), European Centre for Medium-Range Weather Forecasts (ECMWF), cloud liquid water content (LWC), cloud base temperature

1. Introduction

Radiation budget at the Earth's surface is a key factor in various weather phenomena, since it has a direct impact on the large-scale flow and also the ocean and atmospheric boundary layer (Lee et al., 2002). Recent greenhouse gas emissions increase and associated global warming have resulted in the radiation budget changes at the Earth's surface. Therefore, various ground-based observation networks, such as the Baseline Surface Radiation Network (BSRN) (Ohmura et al., 1998), Integrated Surface Irradiance Study (ISIS) (Hicks et al., 1996), SURFace Radiation Budget Network (SURFRAD) (Augustine et al., 2000), and Atmospheric Radiation Measurement (ARM) program (Stokes and Schwartz, 1994) have been established and employed to the studies about surface radiation budget.

Satellite observation can produce high-resolution data across large areas compared to ground-based observation. Since the 1980s, various methods have been proposed for calculating radiation elements based on satellite observation data. Algorithms that estimate the surface solar radiation are as follows. Tarpley (1979) developed a regression equation that predicts hourly surface solar radiation using solar zenith angle, brightness, fractional cloud amount, and other satellite products. The result was a 10% average error compared to ground observation data accumulated daily using pyranometers. Gautier et al. (1980) developed a physical model that considers the cloud effect, water vapor absorption, and Rayleigh scattering under clear and cloudy conditions from the GOES satellite with an average error of 9% with respect to pyranometer data. For the surface thermal radiation, algorithms were developed by Darnell et al. (1983, 1986), Schmetz et al. (1986), Frouin and Gautier (1988), Gupta et al. (1989, 1992, 1993, 1999), and Lee (1993). Recently, Lee et al. (2002) introduced a unique nonlinear statistical model of the DLR estimation method through satellite observations and derived a root mean square error (RMSE) of 9 Wm^{-2} under clear sky conditions and an RMSE of 4-8 Wm^{-2} under overcast conditions depending on the cloud level. Santos et al. (2011) have applied the nine existing atmospheric emissivity equations involved with DLR to the DLR estimation and compared them with observational data in the region of Northeast Brazil. They found the atmospheric emissivity equation that is most appropriate for Brazil's northeast region, yielding a DLR error of less than 1.0%.

The method of calculating radiation elements using empirical models and satellite observation data is efficient in terms of calculation time and accuracy (Fung et al., 1984). Gupta (1992, 1997) derived the clear sky DLR with a small dif-

Corresponding Author: Kyu-Tae Lee, Research Institute for Radiation-Satellite, Gangneung-Wonju National University, Gangwon-do 25457, Korea.
E-mail: ktlee@gwnu.ac.kr

ference of 20-25 Wm^{-2} using an empirical DLR retrieval model. The algorithm is still used to retrieve the DLR of recent satellite sensors like Terra and Aqua/Clouds and the Earth's Radiant Energy System (CERES) (Gupta et al., 1997), and the Geostationary Operational Environmental Satellite R Series satellite (GOES-R)/Advanced Baseline Imager (ABI) (Lee et al., 2010). In this study, the DLR retrieval is performed by calculating cloud base information and applying it to the method of Gupta (1992, 1997).

DLR is one of the factors that can grasp net radiation, so continuous retrieval of DLR is very important, not only under clear sky conditions but also in cloudy sky conditions. Therefore, it is meaningful that the DLR is retrieved by a South Korean satellite and calculated in near real time in all sky conditions.

The 2nd Geostationary Earth Orbit KOrea Multi-Purpose SATellite (GEO-KOMPSAT-2A; GK-2A) from Korea, which is scheduled to launch in May 2018, is equipped with an Advanced Meteorological Imager (AMI) sensor. This sensor has 16 channels and has an overall wavelength range of 0.4-13 μm. Its spatial resolution is 0.5 km or 1 km for visible channels and 2 km for infrared channels. Temporal resolution is 10 min for FD (full disk), ELA (Extended Local Area), and RA (Regional Area) depending on the observation area. There are 52 types of products, including DLR. The calculated DLR could be used for follow-up analysis such as forest fire monitoring and climate analysis, and can be used for data assimilation of weather forecast models.

This study proposes a prototype algorithm for the DLR retrieval of GK-2A, which was performed using various simulation data before GK-2A was launched. The products of GK-2A can be used only after its launch. Therefore, the proposed algorithm can be applied to GK-2A, using the products of GK-2A as input data instead of the simulation data used to develop the proposed algorithm.

2. Research methods and materials

a. Research methods

(1) Definition of surface downward longwave radiation

If atmospheric scattering is neglected, the clear sky DLR of unit wave number at the Earth's surface can be expressed by the following equation (Lee et al., 2010).

$$F_v^{\downarrow} = \pi B_v \, (1 - T(0,z_t)_v) \tag{1}$$

Here, πB_v refers to black body radiation (Wm^{-2}) in accordance with the average atmosphere temperature. B_v is Planck's function and $T(0,z_t)$ is transmittance from the top of atmosphere (z_t) to the Earth's surface ($z = 0$). DLR is the integral of Eq. (1) in the entire wave number of longwave radiation as follows.

$$DLR_{sfc} = \int F_v^{\downarrow} dv = \int \pi B(1 - T(0,z_t)_v) dv \tag{2}$$

In Eq. (2), $1 - T(0,z_t)$ can be expressed as effective emissivity (ε_{eff}) based on the law of energy conservation, and πB can be defined as Planck's function (σT_{eff}^4) by effective emitting temperature (T_{eff}). Consequently, Eqs. (3)-(5) were established.

$$\sigma T_{eff}^4 = \int \pi B_v(T_{eff}) dv \equiv \pi B \tag{3}$$

$$\varepsilon_{eff} \equiv \frac{\int \pi B_v (1 - T(0,z_t)_v) dv}{\int \pi B_v dv} \tag{4}$$

$$DLR = \varepsilon_{eff} \cdot \sigma T_{eff}^4 \tag{5}$$

In other words, Eq. (5) is equivalent to Eq. (2). In this study, DLR was derived based on Eq. (5). The regression coefficients related to ε_{eff} and T_{eff} were calculated using CERES and ERA-interim data.

(2) Calculation of surface downward longwave radiation

DLR was derived based on Gupta (1992, 1997) and expressed as clear sky (DLR_{clr}), cloudy sky ($DLR_{cld,i}$), and cloud cover (CF_i) in Eq. (6). Here, *i* refer to the cloud layer. In other words, DLR is calculated by multiplying the cloud cover by the cloudy sky DLR that was calculated from each vertical atmospheric layer and adding this value to the clear sky DLR of the relevant pixel.

$$DLR = DLR_{clr} + \Sigma_{i=1}^{n} DLR_{cld,i} \times CF_i \tag{6}$$

The clear sky DLR_{clr} in Eq. (6) was calculated as shown in Eq. (7).

$$DLR_{clr} = (A_0 + A_1 V + A_2 V^2 + A_3 V^3) \cdot T_{eff}^{3.7} \tag{7}$$

Here, $V = \ln W$ (W is precipitable water) (mm). T_{eff} is the effective emitting atmosphere temperature (K), and A_0-A_3 are regression coefficients. According to the amount of water vapor in the low troposphere, the effective emitting temperature (T_{eff}) of Eq. (7) for clear sky can be expressed as follows.

$$T_{eff} = K_s T_s + K_1 T_1 + K_2 T_2 \tag{8}$$

Here, T_s refers to the Earth's surface temperature (K). T_1 and T_2 are the average temperature (K) at the Earth's surface-850 hPa and 850-700 hPa, respectively. As weighting functions, K_s, K_1, and K_2 were determined from numerical simulation via the Radiative Transfer Model (RTM).

The cloudy sky DLR_{cld} is a function of cloud base temperature (T_{cb}) and precipitable water (W_c) between clouds and the Earth's surface, as defined by Eq. (9).

$$DLR_{cld} = \frac{T_{cb}^4}{(B_0 + B_1 W_c + B_2 W_c^2 + B_3 W_c^3)} \tag{9}$$

Cloud base temperature (T_{cb}) is represented by absolute

temperature scale (K), and B_0-B_1 are regression coefficients. Eq. (10) (Yoo et al., 2004) was used to determine W_c (mm).

$$W_c \approx \Sigma_{Z_{sfc}}^{Z_b} \times 0.01 \times \overline{q} \times \Delta P \quad (10)$$

Here, $\overline{q}$ is the average specific humidity (g/kg) of the atmospheric layer, and ΔP refers to the pressure difference (hPa) between the upper and lower layers of the atmosphere. Z_b is cloud base height. W_c can be calculated by multiplying 0.01, $\overline{q}$, and ΔP and iteratively summing this product from ground level to cloud base height.

(3) Estimation of cloud base temperature

According to Hutchison et al. (2011), the cloud base temperature (T_{cb}) in Eq. (9) can be calculated using cloud base height (Z_b) and cloud base height is expressed by cloud top height (Z_t) and cloud thickness (ΔZ) as in Eq. (11).

$$Z_b = Z_t - \Delta Z \quad (11)$$

Here, Z_t, Z_b and ΔZ are measured in km. ΔZ can be derived using the empirical method. If cloud top height (Z_t) is less than 4 km, Eq. (12) by Minnis et al. (1992) can be used.

$$\Delta Z = 0.08\tau^{1/2} - 0.04 \quad (12)$$

Here, τ refers to cloud optical depth. In other Cases, cloud top height (Z_t) was calculated by Eq. (13) (Smith Jr. et al., 1993) as a function of cloud top temperature (T_c) and cloud optical depth (τ).

$$\Delta Z = 7.5 - 0.026T_c + 0.85ln\tau \quad (13)$$

When ΔZ < 0.02 km, the ΔZ value is adjusted to 0.02 km and the maximum ΔZ range is 8 km. However, we found that the empirical method of cloud base temperature by Hutchison et al. (2011) using the ratio of cloud liquid water path (LWP) (gm^{-2}) and cloud liquid water content (LWC) (gm^{-3}) can occur a smaller difference compared to the CERES cloud base temperature product in the Case of water clouds. Accordingly, cloud thickness of water clouds (ΔZ_{liq}) can be expressed as follows.

$$\Delta Z_{liq} = LWP/LWC \quad (14)$$

The ratio of LWP with gm^{-2} units to LWC with gm^{-3} units will eventually become physically meter units so that the thickness of water clouds can be known.

For most meteorological satellites, cloud LWC is included in the general output for calculation of Eq. (14). However, other than satellites using Light Detection and Ranging (LiDAR) the cloud LWC calculation is usually not performed due to limitations and low accuracy (Ralph et al., 1954). Therefore, the cloud type classification was utilized for empirical estimation of cloud LWC in this study.

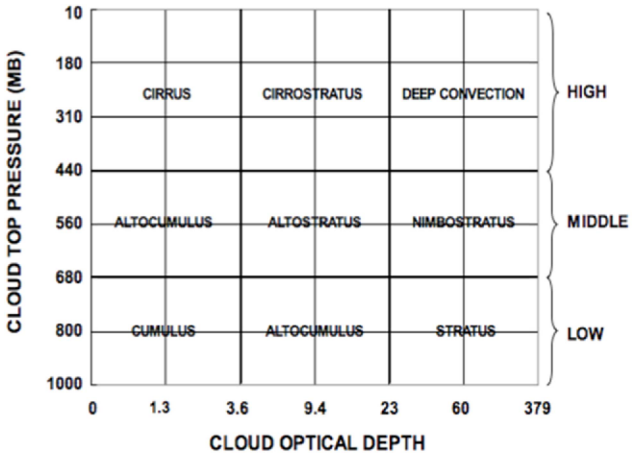

Fig. 1. ISCCP classification of cloud types as a function of cloud optical depth and cloud top pressure (CERES ISCCP - D2like Ed3A Data Quality Summary, 2013).

Table 1. Look-up table of cloud liquid water content according to cloud type.

Cloud Type	LWC [gm^{-3}]
Altocumulus/ Altostratus	0.455
Cirrostratus	0.200
Cirrus	0.025
Cumulus	0.580
Nimbostratus	0.630
Stratus	0.293

Figure 1 shows cloud type classification as a function of cloud optical depth and cloud top pressure according to the International Satellite Cloud Climatology Project (ISCCP) method. The cloud LWC look-up table is presented in Table 1. We utilized the cloud LWC from the Joint Polar Satellite System (JPSS) Visible Infrared Imaging Radiometer Suite (VIIRS) value for stratus, Hutchison et al. (2011) for altocumulus, altostratus, and cumulus, Michael et al. (2015) for cirrus and cirrostratus, and Falcone et al. (1979) for nimbostratus. Exceptionally, we used the Eqs. (12)-(13) in the Case of deep convection water clouds not the look-up table, because of its excellent accuracy.

Figure 2 is a flowchart of the process of calculating DLR in GK-2A. Each pixel is classified into clear sky and cloudy sky. The required preceding products of cloud, surface, and vertical atmospheric information of GK-2A according to each condition is input to the DLR retrieval algorithm described above. The coefficients developed in this study are input together as auxiliary data to calculate DLR. Since the GK-2A satellite has not yet been launched, it is necessary to test the algorithm beforehand and verify its accuracy using other satellites or reanalysis data as simulation data, instead of the preceding products used as input data.

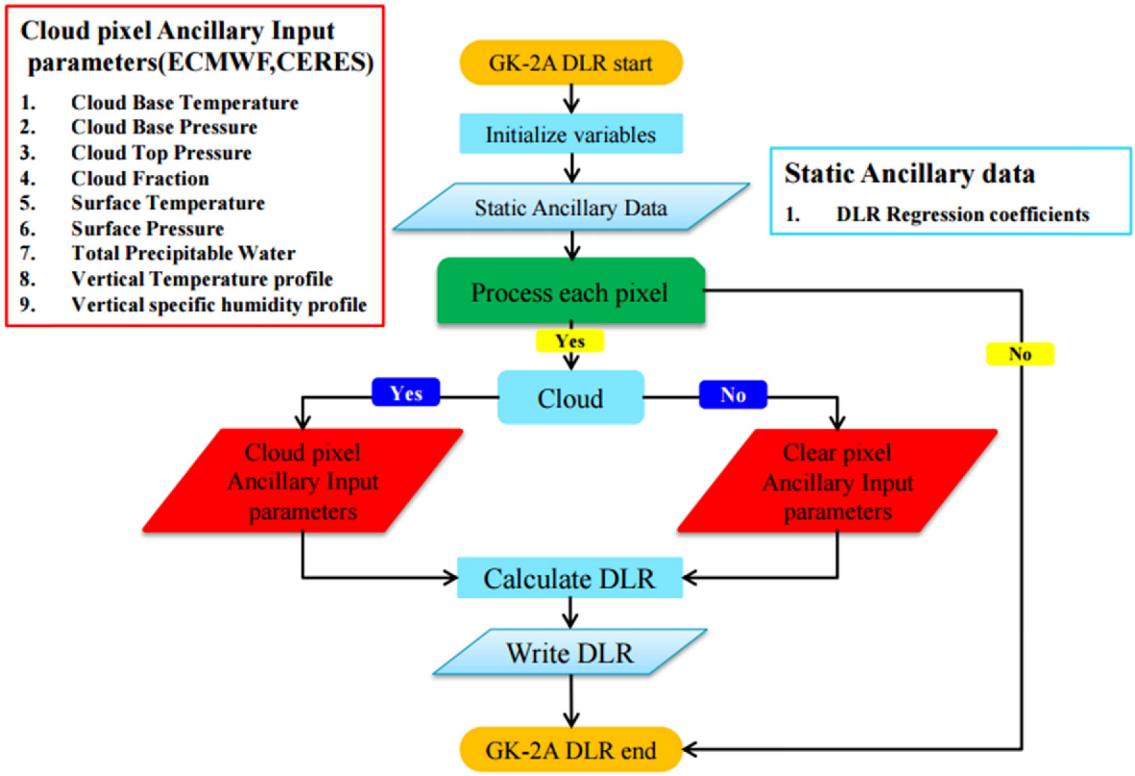

Fig. 2. Flowchart of the Downward Longwave Radiation (DLR) at the surface illustrating the main processing sections.

b. Data

In this study, we used the CERES sensor data mounted on the Terra and Aqua satellites as a part of the National Aeronautics and Space Administration (NASA) satellite project to estimate the radiation budget at the top of the atmosphere and Earth's surface. CERES provides 20 km resolution data within the shortwave region (0.3-5 μm), atmospheric window region (8.1-11.8 μm), and the entire wavelength region (0.3-200 μm). In this study, the cloud-related characteristics were derived using Moderate Resolution Imaging Spectroradiometer (MODIS) data by Minnis et al. (2011), and hourly Single Scanner Footprint (SSF) Edition 4A, Level 3 $1^{o} \times 1^{o}$ resolution data. Not only CERES data but ERA-interim reanalysis data from European Centre for Medium-Range Weather Forecasts (ECMWF) was used. The vertical resolutions of these data consist of 37 layers ranging from 1 hPa to 1000 hPa, and the maximum horizontal resolution is about 8-10 km (Zhou and Wang, 2015). Since the CERES and Era-interim data used in simulations in this study are polar orbiting satellite and reanalysis data, their properties differ from those from GK-2A, which is a geostationary satellite. However, there are advantages in that the cloud and DLR product from CERES can be used for input data and verification respectively, and various temporal and spatial vertical data from ERA-interim can also be utilized.

The CERES and ERA-interim data used in this study are described in Table 2, showing latitude, longitude, and the number of vertical pressure layers. We use the cloud top height, cloud LWP, cloud optical depth and cloud phase referred to CERES (SSF Edition 4A, Level 3) $1^{o} \times 1^{o}$ resolution data in global region for classifying cloud type and calculating cloud base temperature. Here, the cloud phase offers information on a cloud's ice, liquid, or mixed composition in order to apply

Table 2. Input data for DLR algorithm.

Type	Name	Resolution	Dimension
CERES	Cloud Fraction	$1^{o} \times 1^{o}$	(180, 360)
	Cloud Top height	$1^{o} \times 1^{o}$	(180, 360)
	Cloud Liquid Water Path	$1^{o} \times 1^{o}$	(180, 360)
	Cloud Optical Depth	$1^{o} \times 1^{o}$	(180, 360)
	Cloud Phase	$1^{o} \times 1^{o}$	(180, 360)
	Total Precipitable Water	$1^{o} \times 1^{o}$	(180, 360)
ERA-interim	Surface Temperature	$1^{o} \times 1^{o}$	(180, 360)
	Cloud Fraction	$1^{o} \times 1^{o}$	(180, 360)
	Temperature	$1^{o} \times 1^{o}$	(180, 360, 37)
	Pressure Profile	$1^{o} \times 1^{o}$	(180, 360, 37)
	Specific Humidity Profile	$1^{o} \times 1^{o}$	(180, 360, 37)
Development	Cloud Base Pressure	$1^{o} \times 1^{o}$	(180, 360)
	Cloud Base Temperature	$1^{o} \times 1^{o}$	(180, 360)

Table 3. Sample data for DLR calculation.

Case	Date
1	2013.10.02; 0600-0700 UTC
2	2013.10.04; 1800-1900 UTC
3	2014.01.03; 1800-1900 UTC
4	2014.01.06; 0600-0700 UTC
5	2014.04.03; 0600-0700 UTC
6	2014.04.05; 1800-1900 UTC
7	2014.07.01; 0600-0700 UTC
8	2014.07.03; 1800-1900 UTC

Formulas (12)-(14). Because CERES cloud information such as LWP, COD, cloud top height, and cloud phase are provided by layer (high, upper-middle, lower-middle, low), the DLR for each layer can be calculated using Formula (6). GK-2A, which will be applying this algorithm, currently categorizes clouds into three categories (low, mid, high) to calculate cloud phase, but the final DLR algorithm for GK-2A will implement all cloud layers in the future. Vertical temperature, atmospheric pressure, and altitude were obtained from 1° latitude-longitude and 37 vertical layers resolution of ERA-interim reanalysis data to convert cloud base height to temperature and atmospheric pressure.

The DLR product of CERES is relatively accurate data with a bias of 0.2 Wm^{-2} under clear sky conditions and a bias of 5.9 Wm^{-2} under all-sky conditions based on surface observation data (Gupta et al., 2010). In addition, CERES is almost the only data available as simulated data, since near real-time cloud products for the entire earth from satellite-based observation are rare. Therefore, if CERES data is used as the input data and the DLR of CERES is used as the verification data, the accuracy of the new coefficient and cloud base information developed in this study can be verified. Furthermore, in the GK-2A DLR algorithm, the accuracy of the input data will contribute to the accuracy of the DLR retrieval, and the spatial and temporal resolution of the DLR will also depend on the space-time resolution of the input data. The target spatial resolution of the vertical atmospheric profile and precipitable water used as input data for the DLR retrieval algorithm in the GK-2A satellite is less than 10 km, and the spatial resolution of the cloud information and surface temperature is 2 km. In addition, the time resolution is 10 min (full-disk basis). The principle of retrieval for these input data is briefly as follows: cloud information is based on brightness temperature difference calculation; surface temperature is retrieved using the brightness temperature; and the cloud mask, solar zenith angle, latitude/longitude, ocean/land information, and precipitable water are retrieved based on brightness temperature and artificial neural network analysis.

As shown in Table 3, there are eight daytime and nighttime Case studies by season, from autumn 2013 to summer 2014 based on the CERES instrument passing over the East Asia region. To ensure temporal coincidence with the ERA-interim data, the daytime and nighttime Cases utilized CERES 0600-0700 UTC and 1800-1900 UTC data respectively.

c. The process of calculating the coefficients

The coefficients of Formulas (7) and (9) from Gupta (1992), particularly the coefficient regarding cloud sky DLR, are prone to inaccuracy in various situations. However, the DLR of CERES was verified by developing an overall empirical formula. This study utilized the Gupta empirical formula and the Era-interim vertical profile data based on the DLR results from CERES and calculated a new coefficient for the Gupta empirical formula based on the results.

First, when A_0-A_3 are obtained from Formula (7) for clear sky DLR, CERES data is used in DLR_{clr} and V (ln W; W is precipitable water; mm), while Era-interim data is used according to Formula (8) for T_{eff}. Here, the method of Gupta (1992) was followed exactly as is for coefficients Ks-K_2. There were 5,304 data coefficients, and these were input into R to fit Formula (7) and calculate coefficients A_0-A_3. Coefficients B_0-B_3 of the cloudy sky DLRs were calculated using the same method. There were 99,773 data coefficients used, and variable T_{cb} and below-cloud precipitable water W_c were calculated using the CERES cloud data and Era-interim data, and the CERES cloudy sky DLR was used in the left DLR_{cld}.

The RMSE for CERES DLR and the DLR calculated when using Gupta's (1992) coefficient based on all skies was 22.69 Wm^{-2} on average for eight cases, but when the newly calculated coefficient was used, the DLR error decreased to 16.67 Wm^{-2}.

3. Results and analysis of surface downward longwave radiation calculations

For the figures showing the verification results of the calculated DLR in this section, only Cases 1, 3, and 7 are shown as examples because the eight cases in Table 3 had similar results. However, in the full-disk figure for clear sky DLR, only Cases 1 and 7 are shown because the clear pixel count was considerably small in Case 3 and difficult to identify by eye because they were far away. In addition to Cases 1, 3, and 7, the verified scatter plot also shows Case 6, which has the lowest RMSE. Even if the cases were not shown in each figure, their verification results can still be seen in each table.

a. Cloud base temperature

Before showing the verification results for the calculated CBT, the following is a more detailed explanation of the process of calculating CBT. First, if the pixel's cloud fraction value is 0.01, or 1% or higher, it is regarded as cloudy sky in the algorithm, and a CBT calculation is performed. As explained in Chapter 2, since the CBT cannot be calculated directly, the vertical atmospheric profile data is used to convert

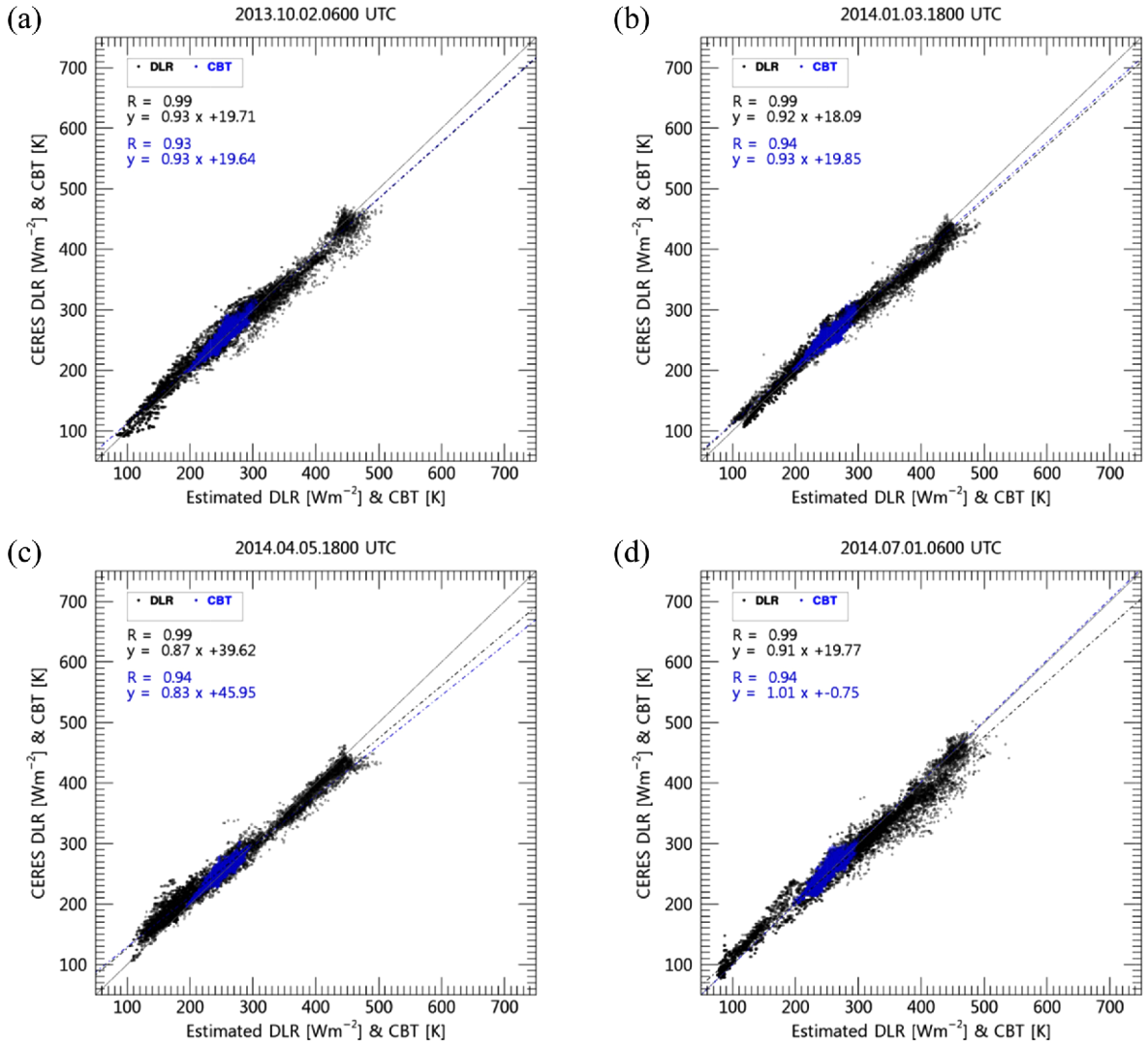

Fig. 3. Scatter plots of retrieved and CERES DLR (black) and retrieved and CERES cloud base temperature (blue) for Cases 1 (a), 3 (b), 6 (c), and 7 (d) in cloudy skies.

the cloud base height into cloud base temperature. When doing this, if the vertical elevation map of Era-interim does not match the elevation map of the calculated cloud base height, the cloud base temperature is calculated using the elevation and temperature right above and below the relevant elevation from Era-interim to create a linear interpolation. Furthermore, the below-cloud precipitable water information required for Formula (9) is calculated by repeatedly accumulating the product of each layer's atmospheric pressure difference and specific humidity from the index to the cloud base height, as in Formula (10). The cloud base height is calculated by subtracting the cloud thickness from the cloud top height that is calculated from the satellite, and Formulas (11)-(14) shown above calculate cloud thickness. If the cloud is composed of water, the highly accurate formula (14) is used, and if it is composed of ice crystals or has a mix of water and ice crystals, empirical formulas (11) or (12) are used depending on the cloud to height. The LWC and LWP are required to calculate the thickness of a cloud composed of water; LWP is calculated from most satellites including CERES and GK-2A, and LWC can be predicted through a chart that uses cloud top pressure and cloud optical depth, as shown in Fig. 1. In this study, because the product of each atmospheric layer's cloudy sky DLR and the cloud fraction is added to the clear sky DLR for a given pixel, as in Formula (6), there may be up to four DLR_{cld} per pixel or cloud base temperature. This is because the cloud-related products of CERES are composed according to low, mid-low, mid-high, and high layers. The final all-sky DLR of the pixel is calculated through this process.

Cloud base temperature is required for cloudy sky DLR calculation. Figure 3(blue) shows cloud base temperatures calculated by Eqs. (12)-(14) and CERES data in Cases 1, 3, 6, and 7, with statistical analysis of the data shown in Table 5. Furthermore, cloud base temperatures were calculated from

Table 4. Regression coefficients for DLR in clear and cloudy skies.

Condition	Coefficient	Value
Clear sky	A_0	1.5414×10^{-7}
	A_1	1.5151×10^{-8}
	A_2	9.5692×10^{-9}
	A_3	-1.3501×10^{-9}
Cloudy sky	B_0	6.4151×10^{7}
	B_1	9.7496×10^{5}
	B_2	5.1418×10^{4}
	B_3	-1.3011×10^{3}

Table 5. Statistical analysis of retrieved and CERES cloud base temperatures.

Case	Number	R	RMSE [K]	Bias [K]
1	30,356	0.93	6.89	−1.86
2	31,441	0.93	6.67	−1.57
3	18,349	0.94	6.05	−1.41
4	27,058	0.94	6.37	−0.87
5	31,790	0.91	7.48	−2.20
6	25,838	0.94	6.98	−4.26
7	29,042	0.94	7.03	−0.89
8	29,773	0.95	6.60	−1.04

Table 6. Statistical analysis of retrieved and CERES DLR in all skies.

Case	Number	R	RMSE [Wm^{-2}]	Bias [Wm^{-2}]
1	13,212	0.99	15.08	−1.06
2	13,930	0.99	14.00	−3.88
3	10,719	0.99	14.25	2.96
4	13,549	0.99	17.79	−7.00
5	14,595	0.99	19.20	−9.25
6	10,890	0.99	19.46	−8.88
7	13,430	0.99	17.45	4.05
8	13,752	0.99	16.14	1.24
Average	13,009.63	0.99	16.67	−2.73

four cloud types from the CERES: high (> 300 hPa), upper-middle (300-500 hPa), lower-middle (500-700 hPa), and low clouds (< 700 hPa). When the four layers of cloud were present at the same point (pixel), the cloud base temperature was calculated for each cloud type. Thus, there are more data items in Fig. 3 and Table 5 than for the all sky data in Table 6.

As shown in Fig. 3, the calculated cloud base temperatures in this study varied within the range 200-300 K depending on latitude, longitude, and cloud characteristics. In Cases about Fig. 3, the correlation coefficients with CERES were greater than 0.93. Table 5 shows the number of cloud base temperature calculations, correlation coefficient, RMSE, and bias for the eight Cases. Since the number of calculations in this table was determined using a maximum of four levels of cloud present at the same point, it reflects the calculation number of total cloud base temperature of all levels. The eight Cases, including the Cases in Fig. 3, showed a correlation coefficient greater than 0.91. In addition, the differences between the DLR calculation and CERES data might be a result of the RMSE for CERES cloud base temperature of about 6-8 K and the negative bias values shown in all Cases.

The error in cloud base temperature estimation for mixed cloud or ice cloud was relatively large compared to that for water clouds. Thus, estimation of cloud ice water content (IWC) is required in order to estimate the cloud base temperature of clouds containing ice crystals. Cloud IWC depends on ice crystal geometry and temperature. It can be estimated through LiDAR observations, but the spatial and temporal resolutions are limited and the accuracy is low as mentioned in Section 2. Accordingly, the empirical method through Eqs. (12)-(14) was used to calculate cloud base temperature.

For ice clouds, empirical Formulas (12)-(13) are unable to fully reflect the various forms of ice crystals. Therefore, Figure 4 shows that there is a considerably large CBT calculation error for ice crystal clouds compared to water clouds. This is a verification scatter plot of the retrieved CBT for middle-low and middle-high clouds using CERES cloud information for Case 1, as an example. Clouds in the middle layer of the atmosphere are a mixture of ice and liquid. In the Case of clouds composed of ice, the CBT retrieval accuracy is remarkably reduced. This difference is attributable to ice crystal clouds that are at the border of cumulonimbus clouds, particularly anvil clouds, in low latitude regions. In other words, when error was compared with CERES DLR after dividing the cloudy sky DLR for all cases into the cumulonimbus range, including anvil clouds, and regions aside from the cumulonimbus range (e.g., cumulus, stratus), the average correlation coefficients were 0.95 and 0.99, respectively. Moreover, the average RMSE values were 20.08 and 16.92 Wm^{-2}, respectively, showing that the DLR error was considerably large in the cumulonimbus range. The low latitudes, particularly in the equatorial region, have very high tropopause altitudes and are therefore a very appropriate condition for growing clouds composed of ice. In fact, many ice clouds are seen in the equatorial region from the Cloud-Aerosol Lidar and Infrared Pathfinder *Satellite* Observations (*CALIPSO*) satellite (Yoshida et al., 2010). Figure 5 shows the verification of DLR calculated by clarifying low-latitude (0^o to $\pm 45^o$) and high-latitude (45^o to 90^o, -45^o to -90^o) for Cases 1, 3, 6 and 7. Aside from Cases 5 and 6, the RMSE of the low latitude all-sky DLR in all cases was greater than the error of the high latitude all-sky DLR. Based on the average of all cases, the accuracy of the all-sky DLR at high latitudes was as high as the RMSE difference of approximately 4.95 Wm^{-2}. It can be seen that the average DLR is high in the low latitude region, and in accordance with Fig. 4, it is understood that the retrieval accuracy of DLR is lowered by the ice clouds at low latitudes.

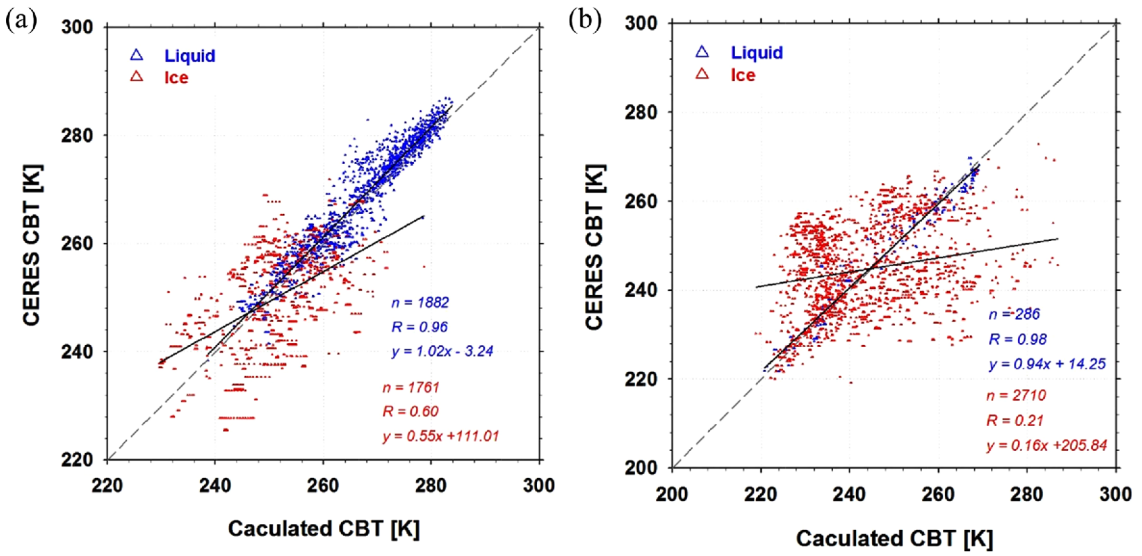

Fig. 4. Scatter plots of retrieved and CERES cloud base temperature of middle-low (a) and middle-high clouds (b) for Case 1.

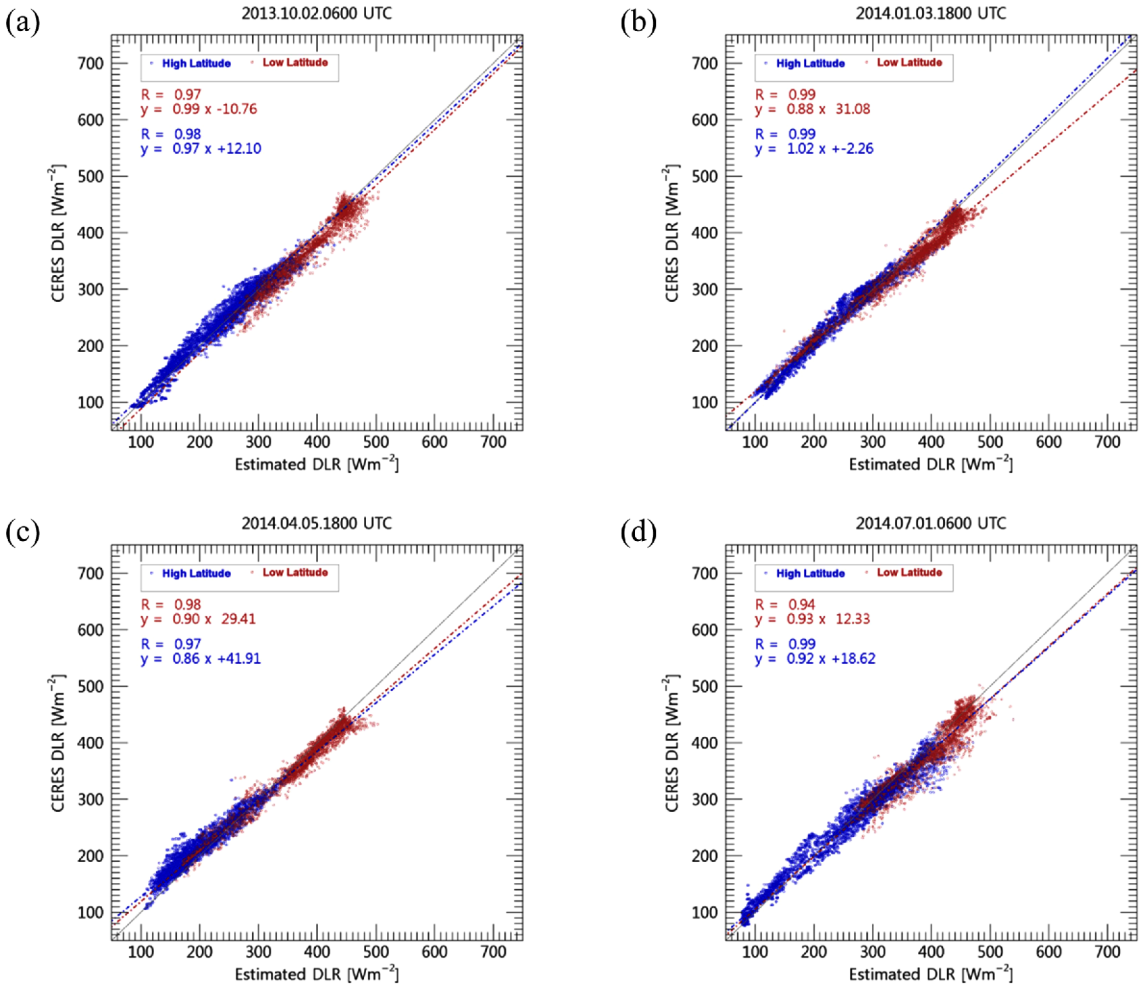

Fig. 5. Scatter plots of retrieved and CERES DLR at high latitudes (45 to 90°, –45 to –90°) (blue) and low latitudes (0° to ± 45°) (red) for Cases 1(a), 3(b), 6(c), and 7(d) from Table 3 under all sky conditions.

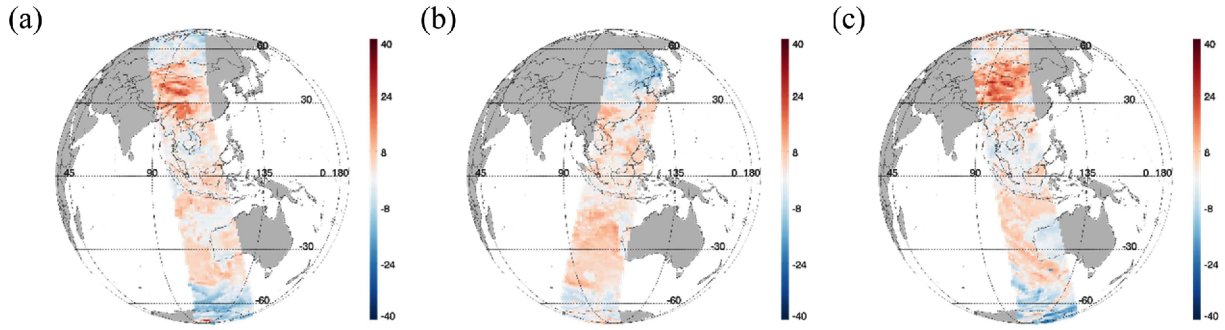

Fig. 6. The percentage difference of retrieved DLR and CERES DLR for Cases 1(a), 3(b), and 7(c) from Table 3 under all sky conditions.

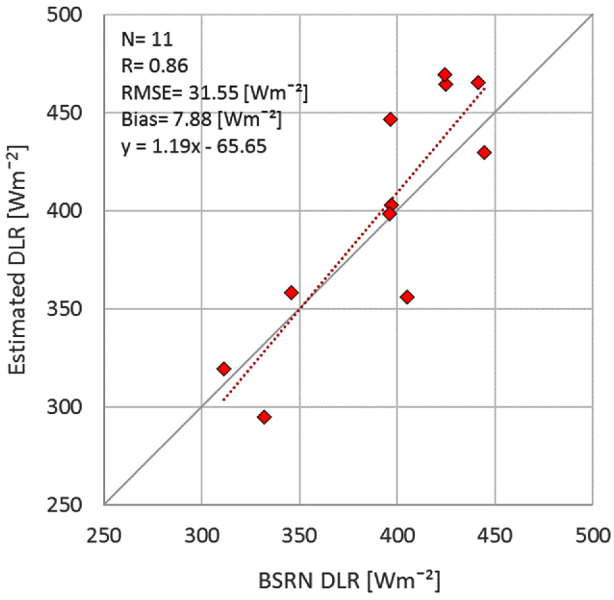

Fig. 7. Scatter plots of retrieved and BSRN DLR for Cases 2, 3, 6, and 8 from Table 3 in all sky conditions.

b. All sky

DLR was calculated according to the Cases in Table 3 and the methods in Section 2. Figure 6 shows the percent difference of CERES DLR and DLR retrieved from the all-sky condition. There is an error of less than 10% in most areas, with up to 40% error in some regions.

The verification scatter plot for Fig. 6 can be seen in Fig. 5 in Chapter 3a. Statistics for the eight Cases in Table 3 are shown in Table 6. The retrieved results were in a good agreement with CERES data, with correlation coefficient (Table 6) greater than 0.99 in all Cases. However, due to the differences in some regions, the average RMSE and bias across the eight Cases were 16.67 Wm^{-2} and −2.73 Wm^{-2}, respectively. The DLR differences were caused by mismatched spatial and temporal resolutions between CERES and the retrieved results, different cloud base temperatures, and amounts of water vapor.

Table 7. Statistical analysis of retrieved and the GWNU LBL model DLR values in clear skies.

Case	Number	R	RMSE [Wm^{-2}]	Bias [Wm^{-2}]
1	443	0.99	12.81	−10.01
2	433	0.99	25.21	−22.49
3	1,764	0.98	31.88	−30.60
4	712	0.99	30.07	−27.27
5	289	0.99	13.51	−10.09
6	193	0.99	9.18	1.43
7	546	0.99	15.64	−10.62
8	924	0.99	17.72	−16.24
Average	663	0.99	19.50	−15.74

The most accurate way to verify the retrieved DLR would be to use surface-based observational data. The time of the case selected in this study is 0600-0700 UTC or 1800-1900 UTC. Tracks in the 0600-0700 UTC time of the CERES sensors mounted on satellites used as input data in this study and the currently operating BSRN observation stations do not overlap. On the other hand, the tracks in the 1800-1900 UTC time of the CERES overlap with the three BSRN stations. Therefore, data from three BSRN stations, Cocos Island (Lat.: −12.19°, Lon.: 96.84°), Ishigakijima (Lat.: 24.34°, Lon.: 124.16°), and Fukuoka (Lat.: 33.58°, Lon.: 130.38°), were used to validate the retrieved DLR. The BSRN limits the uncertainty of the observed DLR data to less than 2%, or 3 Wm^{-2}, which is a very accurate observation (McArthur, 2005). In this study, since DLR is retrieved as the hourly average of 1800-1900 UTC using CERES data, BSRN DLR observation data were also compared by averaging values of 1800-1859 UTC. Figure 7 shows this comparison. The number of data number should total 12 in four cases studies (Cases 2, 3, 6, 8) and three stations, but there are actually 11 data points because there is no data in Case 6 for the Cocos Island station. The latitude-longitude differences between retrieved DLR and BSRN stations is in the range of 0.08-0.16° in latitude and 0.34-5.88° in longitude. These are likely to cause errors in verification.

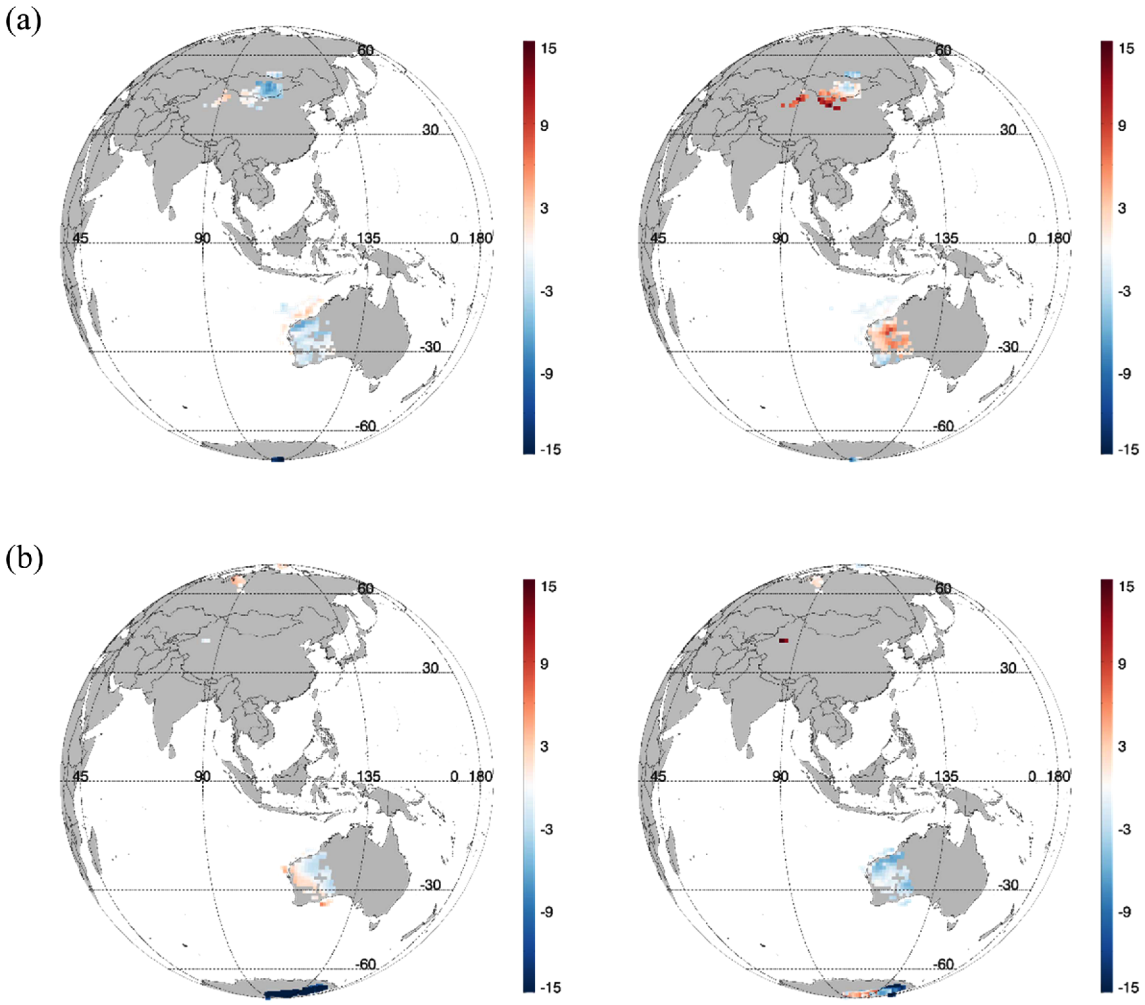

Fig. 8. The percentage difference of retrieved DLR and LBL DLR (left), and CERES DLR (right) for Case 1(a) and 7(b) in clear skies.

The correlation coefficient is about 0.86, so the algorithm used in this study is relatively accurate. RMSE and Bias are overestimated by 31.55 and 7.88 Wm^{-2}, respectively, and the errors are slightly higher than those of CERES (refer to Table 7). However, if the number of experimental cases increases, these errors can be expected to decrease. We plan to test more cases in the future, and this will be a more reliable verification because the amount of data that can be verified also increases.

c. Clear sky

The calculated clear sky DLR values were compared with the RTM - the Gangneung-Wonju National University (GWNU) line-by-line (LBL) model and CERES data. The GWNU LBL model was developed by the Radiation Laboratory of Gangneung-Wonju National University. Under clear sky conditions, numerical simulations of radiation reaching the Earth's surface from GWNU LBL model calculation were consistent with those of 15 models from advanced countries, with differences of less than 1% (Yoo et al., 2007). LBL is calculated in detail between wave numbers and thus has high accuracy. It is the standard model and is able to verify other radiation models (Clough et al., 1992). GWNU LBL calculates the penetration ratio that changes according to greenhouse gases such as CO_2, N_2O, and CH_4 that are input as constants, ozone, evaporation, temperature, and atmospheric pressure in various atmospheric layers. It calculates the upwelling and downwelling flux from each atmospheric layer, radiance, and cooling rate. The formula that is typically used in flux calculations for GWNU LBL was implemented (Clough et al., 1992). Formulas (15) and (16) refer to the upwelling and downwelling flux regarding atmospheric layer l and wave number v, respectively.

$$F^{+}_{v;l} = B_v(\theta_s)T_{v;l,0} + \Sigma^{0}_{l'=l}B_v(\theta)\cdot[T_{v;l,l'} - T_{v;l,l'-1}] \quad (15)$$

$$F^{-}_{v;l} = \Sigma^{L}_{l'=l}B_v(\theta)\cdot[T_{v;l,l'} - T_{v;l,l'+1}] \quad (16)$$

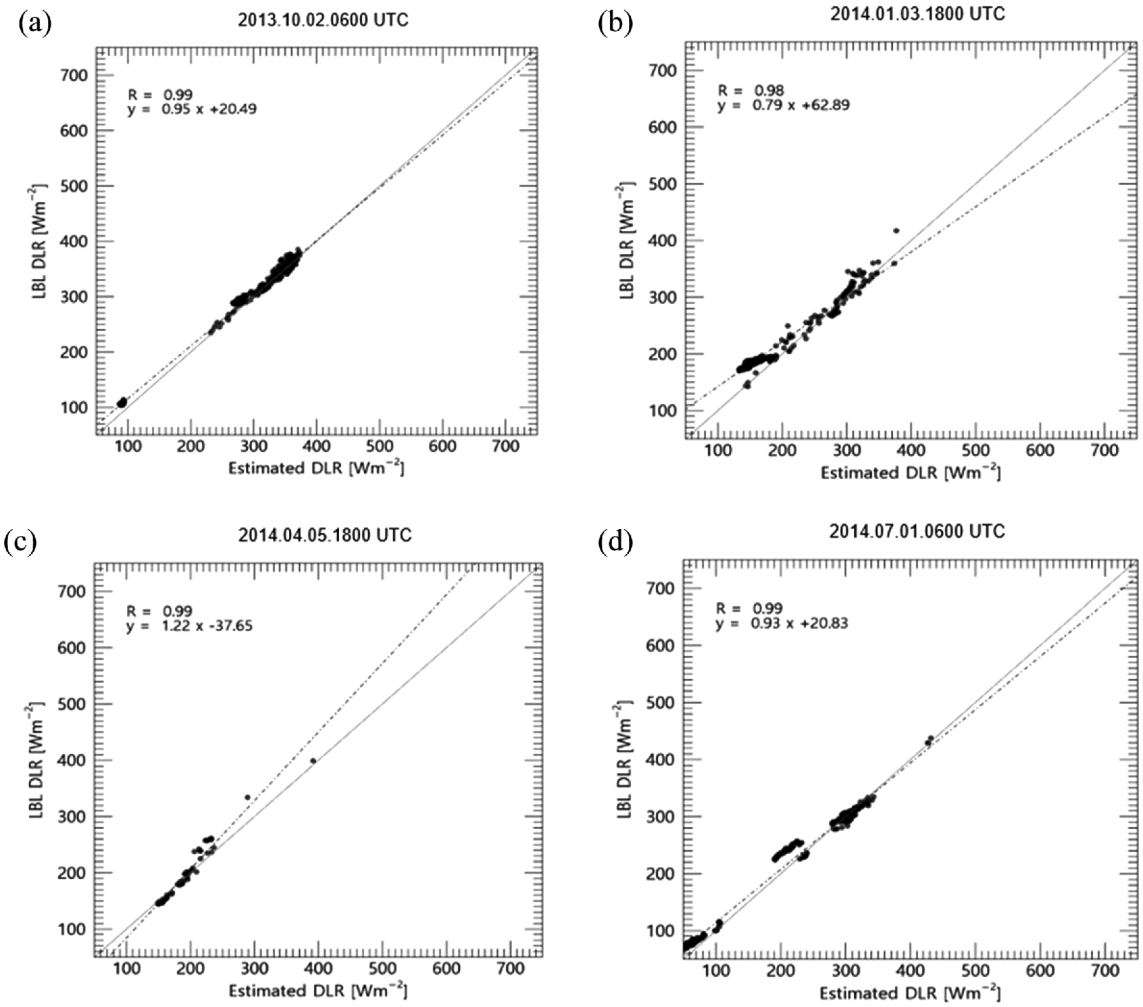

Fig. 9. Scatter plots of retrieved and the GWNU LBL model DLR for Cases 1 (a), 3 (b), 6 (c), and 7 (d) in clear skies.

Here, B is the Planck function, T is the transmittance, L is the surface, 0 is the top of atmosphere, and θ is the temperature. L and 0 are the lowest and highest layers of the pressure that is inputted into the LBL model.

The DLR of the GWNU LBL that is used as verification data in this study used the downwelling flux from the model's lowest layer. For the HIgh resolution TRANsmission molecular absorption (HITRAN) data that correlates to the penetration and absorption of gas molecules, the 2012 version was used because it included gas absorption lines. The absorption line cut-off, which limits the expansion of the absorption line through gas molecules in a given wavelength, was assumed to be 10 cm^{-1}. In terms of wavelength range, the infrared light wavelength range was set to 5-200 μm and tested accordingly. The ERA-interim reanalysis data for each pixel of clear sky were used as inputs of GWNU LBL model, such as vertical atmospheric pressure and temperature, specific humidity, and ozone. Referring to Hecht et al. (1998), the inputs for atmospheric CO_2, N_2O and CH_4 concentrations were 350 ppm, 280 ppb, and 1,750 ppb, respectively.

As shown in Fig. 8, which shows the percent error of LBL and retrieved clear sky DLR, most error was under 5%, and the calculated clear sky DLR values for Cases 1 and 7 were similar to those of CERES and the GWNU LBL model. Although there is a large DLR difference in the results of this study and the LBL model at the South Pole area of this figure, this is due to the artificial zenith angle and is thus not a significant issue. Since the differences are not immediately apparent from the global maps shown in Fig. 8, the results from this study and GWNU LBL model calculations for Cases 1, 3, 6, and 7 are shown as scatter plots in Fig. 9. Although little data was available for clear sky compared to all sky conditions, the scatter plot of the retrieved results for Cases 1, 3, 6, and 7 was in a good agreement with the GWNU LBL model. Statistical analysis of the data is shown in Table 7.

Most of the eight Cases' correlation coefficients were greater than 0.99. Compared with the GWNU LBL model data, the mean RMSE and bias of the DLR retrieved in this study were 19.50 Wm^{-2} and −15.74 Wm^{-2}, respectively. The retrieved results in this study were relatively consistent with the GWNU

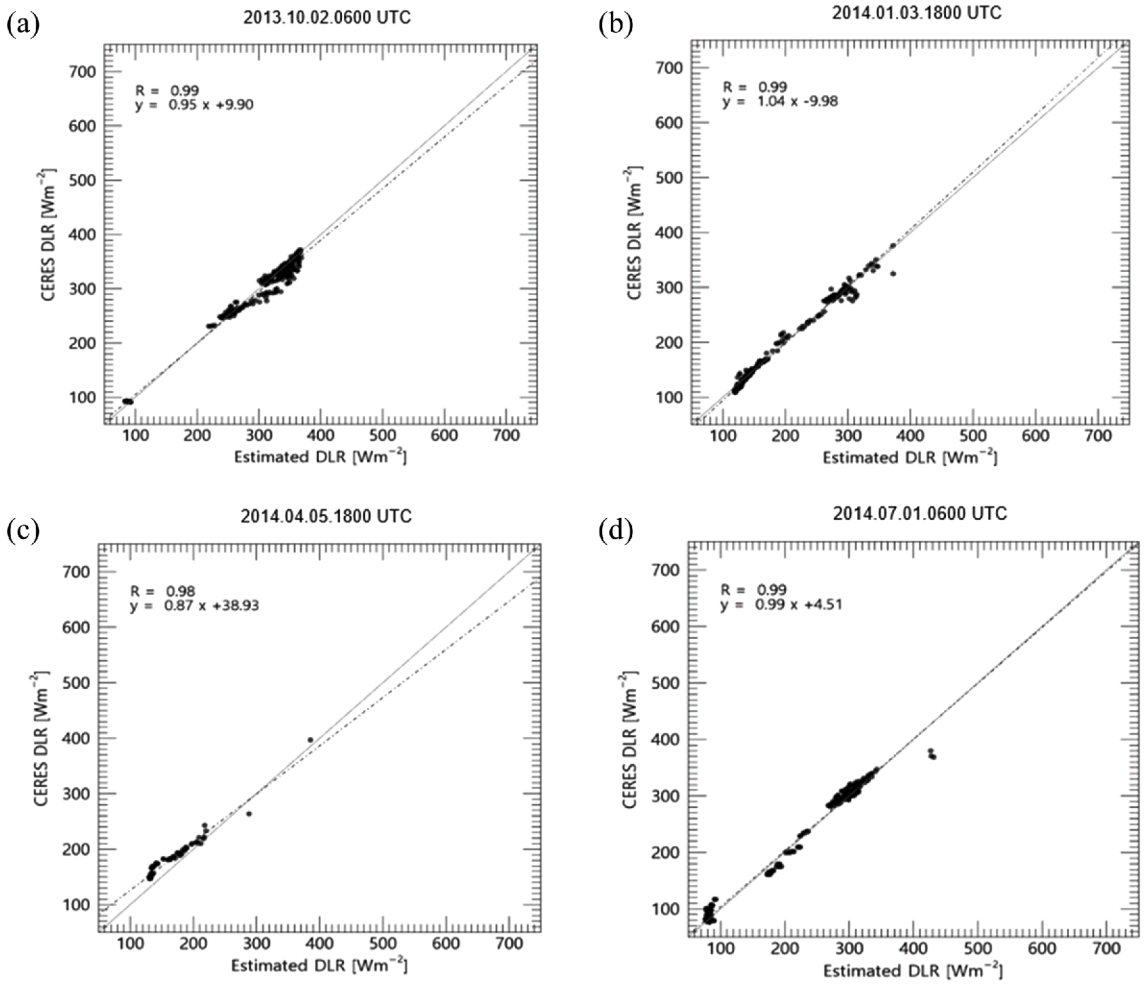

Fig. 10. Scatter plots of retrieved and CERES DLR for Cases 1 (a), 3 (b), 6 (c), and 7 (d) in clear skies.

LBL model calculations. However, the RMSE and bias were greater than those of CERES for all sky conditions (Table 6) in Cases 2-4 and 8. This can be attributed to the difference in space-time resolution between CERES and Era-interim. The spatial grid of CERES SSF Edition 4A, Level 3 data and ERA-interim are as follows: CERES is 89.5 to −89.5°/0.5 to 359.5° (latitude/longitude) with a 1° interval, and Era-interim is 90 to −90° /0 to 359° (Latitude/longitude) with a 1° interval. In addition, the CERES SSF Edition 4A data used in the study is hourly averaged data, which is used to represent 0600-0700 UTC and 1800-1900 UTC at 0600 UTC and 1800 UTC in the study. However, since the Era-Interim analysis data are represented at 0600 UTC and 1800 UTC, there is a slight difference in the space-time resolution. When the CERES represents the midpoint of an hourly average, i.e. 0630 UTC or 1830 UTC, there is a difference of about 30 min from the Era-interim. In some cases, the RMSE error in the clear sky condition is greater than that of the all sky condition. The CERES data is used for the input and verification of the DLR calculation in the all sky condition. On the other hand, in the clear sky condition, CERES and Era-interim data are input for DLR retrieval, but the GWNU LBL model used for verification only uses Era-interim data (temperature·pressure·ozone profile and surface temperature) as input. The comparison and verification of the retrieved results and CERES DLR in clear sky conditions for the same Cases are shown in Fig. 10 and Table 8. There, most of the correlation coefficients between retrieved results and CERES data were greater than 0.99, similar to the findings for the GWNU LBL model, whereas RMSE and bias were significantly improved. There were much little simulation data compared to the all sky conditions in Table 6, but no significant difference was found compared to the GWNU LBL model and CERES results. However, due to the problems of mismatched spatial and temporal resolutions with CERES output and input data of GWNU LBL model the small difference occurred. Therefore, in future studies, we need to conduct precise and comparative analysis with the Himawari-8/ Advanced Himawari Imager (AHI) and GOES-R/ABI data.

Table 8. Statistical analysis of retrieved and CERES DLR in clear skies.

Case	Number	R	RMSE [Wm^{-2}]	Bias [Wm^{-2}]
1	443	0.99	10.25	0.94
2	433	0.99	6.90	2.14
3	1,764	0.99	6.13	4.47
4	712	0.99	7.14	3.65
5	289	0.99	11.60	–4.33
6	193	0.98	20.95	–19.71
7	546	0.99	9.95	–2.86
8	924	0.99	8.24	–1.76
Average	663	0.99	10.14	–2.18

Table 9. Statistical analysis of retrieved and CERES DLR in cloudy skies.

Case	Number	R	RMSE [Wm^{-2}]	Bias [Wm^{-2}]
1	12,769	0.99	15.22	–1.13
2	13,497	0.99	14.17	–4.07
3	8,955	0.99	15.35	2.66
4	12,837	0.99	18.20	–7.59
5	14,306	0.99	19.32	–9.35
6	10,697	0.99	19.43	–8.68
7	12,884	0.99	17.70	4.34
8	12,828	0.99	16.57	1.46
Average	12,346.62	0.99	16.99	–2.80

d. Cloudy sky

To accurately determine the effect of clouds, the remaining all-sky pixels (apart from clear sky) were categorized into cloudy sky for each case, and the analysis was performed accordingly. The DLR calculation results based on cloud base temperature in this study and CERES values in cloudy sky are presented in Fig. 3 (black) and Table 9. The bias of CBT calculations by this study and CERES were negative all of the eight Cases. Accordingly, the cloudy sky DLRs were slightly lower than those of CERES, except for three Cases (Case 3, 7 and 8). The remaining three Cases showed positive DLR bias. This can be interpreted as a result of the fact that the vertical atmospheric profile Era-interim data used in this study is different from the data used in CERES. Cases 5, 6, and 7, which had the highest RMSEs of CBT in Fig. 3, had higher RMSEs (17.70-19.43 Wm^{-2}) for the cloudy sky DLR compared to other cases.

The average RMSE of cloudy sky DLR retrieved in this study and CERES was 16.99 Wm^{-2} for the eight Cases, which was higher than the 10.14 Wm^{-2} obtained for clear sky conditions.

Nevertheless, the reliability of the presented algorithm in this study could be improved by reducing the significant error result from mismatched spatial and temporal resolutions between the ECMWF ERA-interim data employed to calculate cloud base temperature and amount of water vapor under clouds and the CERES data. Thus, a comparative study utilizing the AHI or ABI high-resolution input data should be performed to improve the accuracy of DLR calculation in the future.

4. Discussion and Conclusions

The Earth's surface radiation budget has a significant impact on the analysis of the climatic system and various weather phenomena in the atmosphere and oceans. DLR, which is a component of the Earth's surface radiation budget, has been determined through computational studies using data from meteorological satellite for several decades. However, such calculations are difficult in cloudy sky conditions. In this study, a DLR retrieval algorithm was developed using CERES and ECMWF ERA-interim data based on the method of Gupta (1992, 1997). Because GK-2A has not been launched yet, we considered that other satellite or reanalysis data are the most suitable for use. The prototype algorithm presented in this study is applied to the GK-2A satellite by simply using the preceding products of GK-2A (e.g. cloud and temperature data) as input data. A minor problem may arise because the CERES and ERA-interim reanalysis data used in the development and the observation geometry of the GK-2A satellite are different (William and Adriano, 2017). However, after the launch of GK-2A, errors are likely to be minimized by testing and adjusting the accuracy of the DLR retrieval accordingly. In eight Case studies, correlation coefficients between DLR retrieved in this study and CERES data were greater than 0.99, and average RMSE was 16.67 Wm^{-2} in all sky conditions. In addition, the correlation coefficient was 0.86 and the RMSE was 31.55 Wm^{-2} when compared with the BSRN surface-based observational data. Although the error is slightly larger than that of CERES, it can be interpreted that we have developed a relatively accurate algorithm based on the high correlation coefficient. It is expected that this error will be reduced if we experiment with more Cases.

As a parameter for calculating cloudy sky DLR, cloud base temperature was calculated by empirically estimating cloud LWC. Despite the limitation on IWC estimation for ice cloud, the correlation coefficient with CERES cloud base temperature was greater than 0.91. In the Case of cloudy sky, the average RMSE of CERES data and DLR retrieved in this study for eight Cases was 16.99 Wm^{-2}, compared with 10.14 Wm^{-2} in clear sky. This was attributed to setting the Earth's surface pressure to a constant of 1,000 hPa for calculating cloud base temperature and the amount of water vapor in the atmosphere, and to the problems of mismatching the spatial and temporal resolutions, $1^{o} \times 1^{o}$ ERA-interim data, and CERES data used in this study. This may also be due to errors in cloud base information detection on clouds composed of ice crystals. Because the method presented in this study is not a DLR

retrieval algorithm itself but a methodology, the observation geometry or characteristics of the GK-2A data and the data used in this study may differ. However, if the products of GK-2A are used as inputs of the algorithm after GK-2A is launched, the discrepancy of space-time resolution among the input data generated in this study will be resolved, and the DLR retrieval error will be reduced. The study of cloud base information in ice cloud could be further developed in the present study later.

Preferentially, the accuracy of the DLR calculation could be improved by utilizing high-resolution input data. The high-resolution data include Himawari-8/ AHI and GOES-R/ABI data. The algorithm used in this study only shows the expected result and is not the final algorithm for GK-2A. It will be finalized through continued research.

Some limitations and issues may arise when applying the algorithm to the satellite. First, since the preceding products of GK-2A are directly used as the algorithm input data, if problems occur in any preceding products, the DLR retrieval may be compromised. GK-2A products are classified into real-time products for weather forecasting as well as non-real-time products for research. Immediate problems will not arise in this situation because DLR falls into the research products category. DLR retrieval errors due to short periods of gap in data will be flagged in order to ensure quality assurance and quality control, and long periods of gap in data can be estimated by statistical methods such as interpolation or averaging. Another limitation is that the retrieved DLR can include prior errors, as it uses the preceding products as input data. These errors should be calibrated by quantitative analysis by testing several cases. Despite these issues, we used the preceding products of GK-2A as inputs given the advantage involved; the products share the same observation geometry and space-time resolution.

Edited by: Soon-Il An

References

Augustine, J. A., J. J. DeLuisi, and C. N. Long, 2000: SURFRAD—A national surface radiation budget network for atmospheric research. *Bull. Amer. Meteor. Soc.,* **81**, 2341-2358.

Clouds and the Earth's Radiant Energy System, cited 2013: CERES_ISCCP-D2like Ed3A Data Quality Summary (11/14/2013).

Cho, H. K., J. Kim, Y. Jung, Y. G. Lee, and B. Y. Lee, 2008: Recent changes in downward longwave radiation at King Sejong Station, Antarctica. *J. Climate*, **21**, 5764-5776, doi:10.1175/2008JCLI1876.1.

Clough, S. A., M. J. Iacono, and J.-L. Moncet, 1992: Line-by-line calculations of atmospheric fluxes and cooling rates: Application to water vapor. *J. Geophys. Res.,* **97**, 15761-15785, doi:10.1029/92JD-01419.

Darnell, W. L., S. K. Gupta, and W. F. Staylor, 1983: Downward longwave radiation at the surface from satellite measurements. *J. Clim. Appl. Meteor.*, **22**, 1956-1960, doi:10.1175/1520-0450(1983)022<1956:DLRATS>2.0.CO;2.

_____, _____, and _____, 1986: Downward longwave surface radiation from sun-synchronous satellite data: Validation of methodology. *J. Clim. Appl. Meteor.,* **25**, 1012-1021, doi: 10.1175/1520-0450(1986)025<1012:DLSRFS>2.0.CO;2.

Donaldson Jr, R. J., 1955: The measurement of cloud liquid-water content by radar. *J. Appl. Meteor. Climatol.,* **12**, 238-244, doi:10.1175/1520-0469(1955)012<0238:TMOCLW>2.0.CO;2.

Falcone Jr, J. V., L. W. Abreu, and E. P. Shettle, 1979: Atmospheric Attenuation of Millimeter and Submillimeter Waves: Models and Computer Code. No. AFGL-TR-79-0253, 76 pp.

Frouin, R., C. Gautier, and J.-J. Morcrette, 1988: Downward longwave irradiance at the ocean surface from satellite data: Methodology and in situ validation. *J. Geophys. Res.,* **93**, 597-619, doi:10.1029/JC093iC-01p00597.

Fung, I. Y., D. E. Harrison, and A. A. Lacis, 1984: On the variability of the net longwave radiation at the ocean surface. *Rev. Geophys.*, **22**, 177-193, doi:10.1029/RG022i002p00177.

Gautier, C., G. Diak, and S. Masse, 1980: A simple physical model to estimate incident solar radiation at the surface from GOES satellite data. *J. Appl. Meteor.,* **19**, 1005-1012, doi:10.1175/1520-0450(1980)019<1005:ASPMTE>2.0.CO;2.

Gupta, S. K., 1989: A parameterization for longwave surface radiation from sun-synchronous satellite data. *J. Climate*, **2**, 305-320, doi:10.1175/1520-0442(1989)002<0305:APFLSR>2.0.CO;2.

_____, A. C. Wilber, and W. L. Darnell, 1992: A parameterization for longwave surface radiation from satellite data: Recent improvements. *J. Appl. Meteor. Climatol.,* **31**, 1361-1367.

_____, _____, _____, and J. T. Suttles, 1993: Longwave surface radiation over the globe from satellite data: An error analysis. *Int. J. Remote Sens.,* **14**, 95-114, doi:10.1080/01431169308904323.

_____, _____, C. H. Whitlock, and N. A. Ritchey, 1997: An Algorithm for Longwave Surface Radiation Budget for Total Skies. Cloud and the Earth's Radiant Energy System (CERES) Algorithm Theoretical Basis Document. CERES ATBD Subsystem 4.6.3, Release 2.2, 21 pp.

_____, _____, _____, _____, P. W. Stackhouse Jr, and G. G. Gibson, 1999: A climatology of surface radiation budget derived from satellite data. *J. Climate,* **12**, 2691-2710.

_____, _____, D. P. Kratz, T. Zhang, P. W. Stackhouse Jr, T. Zhang, and V. E. Sothcott, 2010: Improvement of surface longwave flux algorithms used in CERES processing. *J. Appl. Meteor. Climatol.*, **49**, 1579-1589, doi:10.1175/2010JAMC2463.1.

Hecht, J. E., and B. Orlando, 1998: Can the Kyoto protocol support biodiversity conservation? Legal and financial challenges. *Environ. Law Rep. News Anal*., **28**, 10508-10518.

Hicks, B. B., J. J. DeLuisi, and D. Matt, 1996: The NOAA Integrated Surface Irradiance Study (ISIS): A new surface radiation monitoring network. *Bull. Amer. Meteor. Soc.,* **77**, 2857-2864, doi:10.1175/1520-0477(1996)077<2857:TNISIS>2.0.CO;2.

Hutchison, K., A. Huang, and E. Wong, 2011: Joint Polar Satellite System (JPSS) VIIRS Cloud Base Height Algorithm Theoretical Basis Document (ATBD). Joint Polar Satellite System (JPSS) Ground Project. Code 474, 35 pp.

Kato, S., and N. G. Loeb, 2005: Top-of-atmosphere shortwave broadband observed radiance and estimated irradiance over polar regions from Clouds and the Earth's Radiant Energy System (CERES) instruments on Terra. *J. Geophys. Res.*, **110**, D07202, doi:10.1029/2004JD005308.

Lee, H.-T., and R. G. Ellingson, 2002: Development of a nonlinear statistical method for estimating the downward longwave radiation at the surface from satellite observations. *J. Atmos. Oceanic Technol.,* **19**, 1500-1515, doi:10.1175/1520-0426(2002)019<1500:DOANSM>2.0.CO;2.

_____, I. Laszlo, and A. Gruber, 2010: Advanced Baseline Imager (ABI) Earth Radiation Budget - Downward Longwave Radiation: Surface (DLR). Algorithm Theoretical Basis Document. Version 2, 41 pp.

Loeb, N. G., and Coauthors, 2003: Angular distribution models for top-of-atmosphere radiative flux estimation from the Clouds and the Earth's

Radiant Energy System instrument on the Tropical Rainfall Measuring Mission Satellite. Part I: Methodology. *J. Appl. Meteor. Climatol.*, **42**, 240-265, doi:10.1175/1520-0450(2003)042<0240:ADMFTO>2.0.CO;2.

_____, and Coauthors, 2005: Angular distribution models for top-of-atmosphere radiative flux estimation from the Clouds and the Earth's Radiant Energy System instrument on the Terra satellite. Part I: Methodology. *J. Atmos. Oceanic Technol.*, **22**, 338-351, doi:10.1175/JTECH1712.1.

Loeb, N. G., K. J. Priestley, D. P. Kratz, E. B. Geier, R. N. Green, B. A. Wielicki, P. O. R. Hinton, S. K. Nolan, and D. R. Doelling, 2007: Angular distribution models for top-of-atmosphere radiative flux estimation from the Clouds and the Earth's Radiant Energy System instrument on the Terra satellite. Part II: Validation. *J. Atmos. Oceanic Technol.*, **24**, 564-584, doi:10.1175/JTECH1983.1.

McArthur, B., 2005: Baseline Surface Radiation Network (BSRN). World Climate Research Programme. WMO/TD-No. 1274, 176 pp.

Michael, A. B., and P. B. Gail, 2015: *Physics of Radiation and Climate*. CRC Press, 513 pp.

Minnis, P., P. W. Heck, D. F. Young, C. W. Fairall, and J. B. Snider, 1992: Stratocumulus Cloud Properties Derived from Simultaneous Satellite and Island-Based Instrumentation During FIRE. *J. Appl. Meteor. Climatol.*, **31**, 317-339, doi:10.1175/1520-0450(1992)031<0317:SCPDFS>2.0.CO;2.

_____, and Coauthors, 2011: CERES edition-2 cloud property retrievals using TRMM VIRS and Terra and Aqua MODIS data-Part I: Algorithms. *IEEE T. Geosci. Remote,* **49**, 4374-4400, doi:10.1109/TGRS.2011.2144601.

Ohmura, A., and Coauthors, 1998: Baseline Surface Radiation Network (BSRN/WRMC): New precision radiometry for climate research. *Bull. Amer. Meteor. Soc.*, **79**, 2115-2136, doi:10.1175/1520-0477(1998)079<2115:BSRNBW>2.0.CO;2.

Santos, C. A. C. D., B. B. D. Silva, T. V. R. Rao, P. Satyamurty, and A. O. Manzi, 2011: Downward longwave radiation estimates for clear-sky conditions over northeast Brazil. *Rev. Bras. Meteorol.*, **26**, 443-450, doi:10.1590/S0102-77862011000300010.

Schmetz, P., J. Schmetz, and E. Raschke, 1986: Estimation of daytime downward longwave radiation at the surface from satellite and grid point data. *Theor. Appl. Climatol.,* **37**, 136-149.

Smith Jr, W. L., P. Minnis, J. M. Alvarez, T. Uttal, J. M. Intrieri, T. P. Ackerman, and E. Clothiaux, 1993: Development of methods for inferring cloud thickness and cloud thickness and cloud-base height from satellite radiance data. *Extended Abstract, The FIRE Cirrus Science Results 1993*, NASA Langley Research Center, 32-35.

Stephens, G. L., M. Wild, P. W. Stackhouse Jr, T. L'Ecuyer, S. Kato, and D. S. Henderson, 2012: The global character of the flux of downward longwave radiation. *J. Climate*, **25**, 2329-2340, doi:10.1175/JCLI-D-11-00262.1.

Stokes, G. M., and S. E. Schwartz, 1994: The Atmospheric Radiation Measurement (ARM) program: Programmatic background and design of the cloud and radiation test bed. *Bull. Amer. Meteor. Soc.,* **75**, 1201-1221, doi:10.1175/1520-0477(1994)075<1201:TARMPP>2.0.CO;2.

Tarpley, J. D., 1979: Estimating incident solar radiation at the surface from geostationary satellite data. *J. Appl. Meteor.*, **18**, 1172-1181, doi:10.1175/1520-0450(1979)018<1172:EISRAT>2.0.CO;2.

William, E., and C. Adriano, 2017: *Introduction to Satellite Remote Sensing: Atmosphere, Ocean, Land and Cryosphere Applications*. Elsevier, 860 pp.

Yoo, C.-S., C.-K. Shin, and Y.-N. Yoon, 2004: Estimation and Analysis of Precipitatable Water. *J. Korean Soc. Civil Eng.*, **24**, 413-420 (in Korean with English abstract).

Yoo, J.-M., and Coauthors, 2007: Intercomparison of shortwave radiative transfer models for a Rayleigh atmosphere. *J. Korean Earth Sci. Soc.*, **28**, 298-310, doi:10.5467/JKESS.2007.28.3.298.

Yoshida, R., H. Okamoto, Y. Hagihara, and H. Ishimoto, 2010: Global analysis of cloud phase and ice crystal orientation from Cloud-Aerosol Lidar and Infrared Pathfinder Satellite Observation (CALIPSO) data using attenuated backscattering and depolarization ratio. *J. Geophys. Res.*, **115**, doi:10.1029/2009JD012334.

Zhou, C., and K. Wang, 2015: Evaluation of surface fluxes in ERA-Interim using flux tower data. *J. Climate*, **29**, 1573-1582, doi:10.1175/JCLI-D-15-0523.1.